

Nanometer-scale microscopy via graphene plasmons

Xiaodong Zeng,^{1,2} M. Al-Amri,^{1,2} and M. Suhail Zubairy¹

¹*Institute for Quantum Science and Engineering (IQSE) and Department of Physics and Astronomy, Texas A&M University, College Station, Texas 77843-4242, USA*

²*The National Center for Applied Physics, KACST, P.O. Box 6068, Riyadh 11442, Saudi Arabia*

(Received 6 July 2014; revised manuscript received 24 November 2014; published 9 December 2014)

Using graphene plasmons (GPs), we can realize a **nanometer-scale microscopy**. Our scheme takes advantage of the **extremely large wave number of GPs** and the **low loss of graphene**. Comparing with **conventional nonlinear structured-illumination microscopy based on high-order nonlinearity associated with high intensity light**, our proposal only requires linear response. Consequently we need a very weak field, which means less damage to the sample and which may play a significantly important role in the imaging of the biological systems.

DOI: [10.1103/PhysRevB.90.235418](https://doi.org/10.1103/PhysRevB.90.235418)

PACS number(s): 78.67.Wj, 42.30.Va, 73.20.Mf

I. INTRODUCTION

The **classical Abbe diffraction limit in fluorescence light microscopy** had been a barrier for obtaining image information with a resolution better than half the wavelength of light for quite a long time. As the frontiers of science and technology approach the nanoscale, defeating the diffraction limit is a prerequisite to get nanometer resolution, especially in the biological area. The past two decades have seen several methods that are capable of resolving structure beyond the diffraction limit [1–17]. However, these subdiffraction techniques suffer from certain shortcomings. For example photoactivated localization microscopy and stochastic optical reconstruction microscopy methods of localizing individual fluorophores in the sample to subdiffraction precision require the generation of a large amount of raw images [8,9]. Similarly, stimulated-emission depletion requires a subdiffraction illumination of light and spot by spot scanning of the sample, which leads to low speed and requires a strong driving laser field [10–12].

Another high-resolution method, the **structured-illumination microscopy (SIM)** has been of special interest [13–16] in recent years. Linear SIM has been realized nearly 20 years ago but with resolution limitation [13,14]. Since these years, nonlinear SIM has become a widely used method to get a high-resolution image, which was first proposed by Heintzmann *et al.* [15] and was implemented experimentally by Gustafsson [16], and so on. In this method, two counterpropagating fields construct a spatially periodic illumination structure. The atoms or molecules have different fluorescence abilities under different light intensities. This dependence is nonlinear rather than the atom or molecule undergoing the multiphoton's process (in practice, nonlinear order is less than four). This generates high spatial frequency information in the far field, hence leading to higher resolution. However, high resolution means higher-order nonlinearity and subsequently high light intensity. This leads to the possibility for damage to the sample and thus limits the use of this kind of microscopy, especially in biological systems. In Ref. [17], the author used metal plasmons to construct a periodical strip pattern, subsequently a microscopy called **plasmon structure-illumination microscopy**. However, due to the limitations of metal plasmons, this method has a small resolution or low precision.

Graphene, a single layer of carbon atoms arranged in a honeycomb lattice, has attracted tremendous interest due to its unique electronic, mechanical, and optical properties [18–34]. The linear dispersion relation near the Dirac point of the energy band induces a special optical response to the light, including high efficiency for light-matter interactions, strong optical nonlinearity, and unusual surface plasmons. Graphene plasmons (GPs) have emerged as a hot topic in recent years due to their new frequency region, tunability, long-lived, and extreme light confinements [20–34]. The Fermi velocity of the doped graphene is $v_F = 10^6$ m/s, which leads to a wave number that is about two orders larger than that in vacuum. Additionally, due to Pauli blocking, doped graphene has a low absorption in the midinfrared region.

In this paper, we use these interesting properties of graphene to set up structured-illumination microscopy in which we use the GPs as the illumination light. In such a system, the effective illuminated field frequency is large even though the real frequency ω is in the midinfrared region. We demonstrate that, by exploiting the weak-field intensity associated with linearity, very large spatial frequency can be mixed to the far field and an increase of more than a hundred times resolution becomes possible.

The paper is organized as follows: In Sec. II, we give our model and scheme. Our simulations and discussion are presented in Sec. III. The last part is the conclusion.

II. THEORY AND SCHEME

In the long wavelength and high doping limit, i.e., $\hbar\omega \ll E_F$ with E_F being the Fermi energy, the in-plane conductivity of graphene can be described by a simple semiclassical local Drude model $\sigma(\omega) = ie^2 E_F / [\pi \hbar^2 (\omega + i/\tau)]$ under the random-phase approximation [31,33]. Here τ describes the momentum relaxation time due to impurity or phonon-mediated scattering. In the special frequency region, it can be expressed as $\tau = \mu E_F / ev_F^2$ where μ is the mobility of the graphene charge carriers. The tunability of the graphene results from the controllability of the Fermi energy, such as by adjusting the temperature or electrostatic gating.

Similar to normal metals having free electrons' collective oscillation, the electron carriers of the doped graphene can also respond to the electromagnetic field resonantly leading to GPs. For a plane dielectric-monolayer graphene-dielectric model,

the plasmon dispersion relation has the following form [26,31]:

$$\begin{aligned} k_{gp}(\omega) &\approx \frac{2\pi\hbar^2\varepsilon_0(\varepsilon_1 + \varepsilon_2)}{2e^2 E_F} \omega^2 (1 + i/\tau\omega) \\ &\approx \frac{(\varepsilon_1 + \varepsilon_2)}{4\alpha} \frac{\omega}{\omega_F} k_0 (1 + i/\tau\omega). \end{aligned} \quad (1)$$

where $\alpha = e^2/4\pi\hbar\varepsilon_0c \approx 1/137$ is the fine-structure constant, $\omega_F = E_F/\hbar$, and k_0 is the vacuum wave number. Here ε_1 and ε_2 are the dielectric permittivity above and below the graphene, respectively. We note that the wave number is about two orders larger than the vacuum wave number and can lead to extremely large subdiffraction capability.

The spatial density of the sample atoms can be decomposed into its spatial Fourier components [13,14],

$$F(x, y) = \iint f(k_x, k_y) e^{ik_x x + ik_y y} dk_x dk_y. \quad (2)$$

As in incoherent fluorescence microscopy, the measured image $M(x, y)$ can be described by a multiplication of the local excitation intensity $I(x, y)$ by the local fluorescence concentration $F(x, y)$, followed by a convolution with the point-spread function $T(x, y)$ of the incoherent imaging system for the emitted field [14],

$$M(x, y) = \iint [F(x', y') P(x', y')] T(x - x', y - y') dx' dy', \quad (3)$$

where $P(x', y') = AI(x', y')$ is the fluorescence ability or population of the excited state. Here, A is a constant and dependent on the characteristics of the atom. In the spatial frequency domain, the image reads $m(k_x, k_y) = t(k_x, k_y)\phi(k_x, k_y)$, where $m(k_x, k_y)$ and $t(k_x, k_y)$ are the corresponding two-dimensional Fourier transformations of $M(x, y)$ and $T(x, y)$. The function $t(k_x, k_y)$ is also called the optical transfer function (OTF). Here $\phi(k_x, k_y)$ is the spatial frequency spectrum [14].

In conventional fluorescence microscopy, only the Fourier components within the passband $\sqrt{k_x^2 + k_y^2} = k_{\parallel} \leq 2\text{NA}k_0 = \kappa$ can be observed as the OTF is nonzero only in this region. Here NA is the numerical aperture. As shown in Fig. 2(a), only the spatial frequencies inside the circle with the center at the origin contribute to the image. The traditional linear SIM uses a structured-illumination pattern and utilizes the so-called “moiré effect” to couple some of the high spatial frequency information from outside of the circle into the circle to improve the resolution. If the illumination field intensity pattern is sinusoidal with period λ_1 , the spatial frequency spectrum has the following form [14]:

$$\begin{aligned} \phi(k_x, k_y) &= 2f(k_x, k_y) + f(k_x - k_1, k_y) e^{i\Delta_x} \\ &\quad + f(k_x + k_1, k_y) e^{-i\Delta_x}. \end{aligned} \quad (4)$$

where $k_1 = 2\pi/\lambda_1$ and Δ_x is the shift of the pattern. Because of the diffraction limit, λ_1 cannot be smaller than $\lambda_0/2$. We can see that the spatial frequency region is enlarged to a circle with radius $\kappa + k_1$. In a real experiment, sometimes we use the objective lens as the illumination source. The wave number k_1 is approximately equal to κ , and the resolution can be extended by a factor of 2 [13,14].

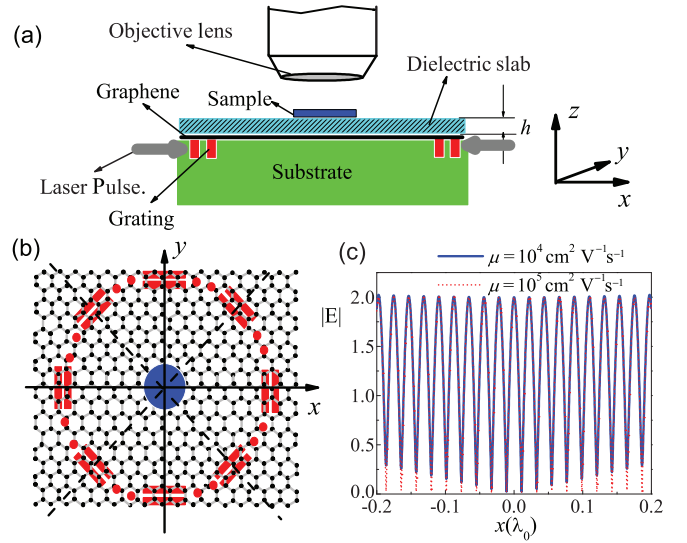


FIG. 1. (Color online) (a) The diagram of the microscopy. A plane monolayer graphene is located between a substrate and a dielectric slab with thickness h . The sample is on the slab. There are gratings in the substrate that can couple the incident laser pulse to the GPs. (b) The top view of the microscopy. There are gratings surrounding the origin. (c) The field amplitude on the plane of the sample along the x axis as the two plasmons propagate along and opposite the x axis. The blue solid line is for the case where $\mu = 10^4 \text{ cm}^2 \text{ V}^{-1} \text{ s}^{-1}$, and the red dotted line is for $\mu = 10^5 \text{ cm}^2 \text{ V}^{-1} \text{ s}^{-1}$. The other parameters are $E_f = 0.6$, $\hbar\omega = 0.2 \text{ eV}$, and $\varepsilon_1 = \varepsilon_2 = 2$. At point $x = 0$, the two plasmons have the same field amplitude.

In our investigation, we use a sample similar to Refs. [15,16]. In these studies, the saturated excitation probability P of the fluorescence atom in Eq. (3) is given by $P = 1 - \Gamma/(\eta I + \Gamma)$, where η is the absorption crossing section and Γ is the decay rate of the atom. It is clear that the fluorescence is nonlinearly dependent on the illumination light intensity with period λ_1 if we choose a large η and a small Γ . The Taylor expansion contains infinite terms. However, only the first several terms can overcome the noise. In vacuum, because of the diffraction effect, the m th-order expansion at most can mix the mk_1 spatial frequency to the far field. For a given atom, if we want to increase the nonlinear effect, the field must be very strong, which can be harmful to the sample.

In the following, we show how to utilize monolayer graphene to design a high-resolution microscopy with a very weak field. Here, we use only linear response and do not consider high-order nonlinearity.

As shown in Figs. 1(a) and 1(b), there is a dielectric slab with thickness h between the graphene and the sample. Since the GPs' intensity decreases exponentially as the distance to the graphene, the electromagnetic field intensity on the sample can be manipulated by optimizing h . In the substrate, dielectric gratings are circular distributions around the sample position. Two laser pulses irradiate the gratings to excite two plasmons [24] (of course, we also can use other methods to generate plasmons [35]). The two plasmons with the same wave number have different propagation directions and can construct a periodic pattern in one dimension. The plasmon can propagate and can be reflected by the gratings on the opposite side and can affect the field pattern. However, the

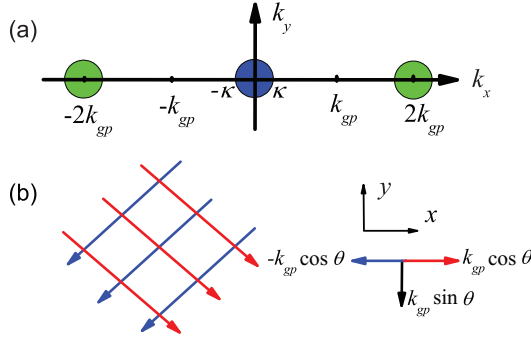


FIG. 2. (Color online) (a) The diagram of the spatial frequency. The blue circle at the origin contributes to the conventional microscopy. The green circles with the center at $\pm 2k_{gp}$ correspond to the linear response of the illumination pattern. (b) Controlling the directions of two GPs, a sinusoidal pattern with effective wave number $k_{gp} \cos \theta$ can be constructed.

coupling between the plasmon and the reflection plasmon is weak due to the wave-vector mismatching. Additionally, the dissipation of the GPs also decreases the reflection plasmon intensity. These two reasons imply that the reflection plasmon affects the field pattern slightly.

In Fig. 1(c), we plot the light intensity along the x axis for different μ 's when the two counterpropagation plasmons are along the x direction. The real parts of the wave numbers are about $45.7k_0$ with a corresponding wavelength of $\lambda_{gp} = 0.0219\lambda_0$, which is tiny compared to that in vacuum. The imaginary parts are $0.246k_0$ and $0.025k_0$ for $\mu = 10^4$ and $\mu = 10^5 \text{ cm}^2 \text{ V}^{-1} \text{ s}^{-1}$, which induce decreases in the plasmon intensity as the plasmon propagates. At the location of the sample, the field intensity pattern along the x axis is almost sinusoidal due to $\text{Im}(k_{gp})$, which is much smaller than $\text{Re}(k_{gp})$. In the following calculation, we do not consider this effect and will analyze it later.

Comparing with the theory in Ref. [16], we can see that, for the linear response, the emitted field contains the information of the $\pm 2k_{gp}$ and $0k_0$ components shown in Fig. 2(a). Using the phase-shift method [16], we can separate the components. In this step, we should change the initial phase of one incident pulse to manipulate the location of the illumination pattern. If we just use linear effect, we need to

move the pattern three times and get three images. However, only with this information, the distribution of the atom cannot be fully reconstructed. In order to obtain the residual Fourier information in the x direction, we can control the direction of the two illumination pulses as shown in Fig. 2(b), which will construct a sinusoidal field pattern in the x -axis direction with an effective period $\pi/k_{gp} \cos \theta$, where θ is the angle between the plasmons and the x axis. By controlling θ , we can extract all the information along the x axis. Similarly, we can obtain all the Fourier components in Eq. (2) with $k_{\parallel} \leq 2k_{gp} + \kappa$ by rotating the x axis around the origin.

III. SIMULATION AND DISCUSSION

Knowing all the Fourier information, an image of the sample can be reconstructed [13–16]. In Fig. 3, we demonstrate the image simulations under different parameters. In these simulations, first, we perform Fourier transformation on the atom distribution function and get the Fourier information $f(k_x, k_y)$; second, we perform inverse Fourier transformation of $f(k_x, k_y)$ within $k_x^2 + k_y^2 \leq 2k_{gp} + \kappa$. Then, we can obtain the high-resolution images. Here, we assume $\text{NA} = 1$. We can see a 68.5 times resolution increase in Fig. 3(b) and a 137 times resolution increase in Fig. 3(c). This shows that we can get a nanometer-scale microscopy by using a midinfrared field.

In the preceding discussion, we did not consider the influence of the dissipation of the GPs on the results. As shown in Fig. 1(c), if we set $\mu = 10^4 \text{ cm}^2 \text{ V}^{-1} \text{ s}^{-1}$, only the area near the spot where the two plasmons have the same amplitude can the illumination pattern be approximated as sinusoidal. At the position away from the spot, the field irradiated on the sample can be considered as the sum of a plane wave and a sinusoidal pattern. Then the observed image has two contributions. The information in the sinusoidal pattern field is contained in all three circles in Fig. 2(a), but the contribution due to the plane field is contained only in the circle located at the origin. It is therefore clear that ignoring the plane-wave contribution may lead to an error. However, this effect has a small influence on our result. For example, in Fig. 4, we simulate the reconstructed image for the case where $\mu = 10^4 \text{ cm}^2 \text{ V}^{-1} \text{ s}^{-1}$. The Fourier components in Eq. (4) are revised to $\iint F(x, y) e^{-2\gamma_y y} e^{-i(k_x - k_1)x} e^{-ik_y y} dx dy$, $\iint F(x, y) e^{-2\gamma_y y} e^{-i(k_x + k_1)x} e^{-ik_y y} dx dy$, and $\iint F(x, y) e^{-2\gamma_y y} (e^{-\gamma_x x} + e^{\gamma_x x})$

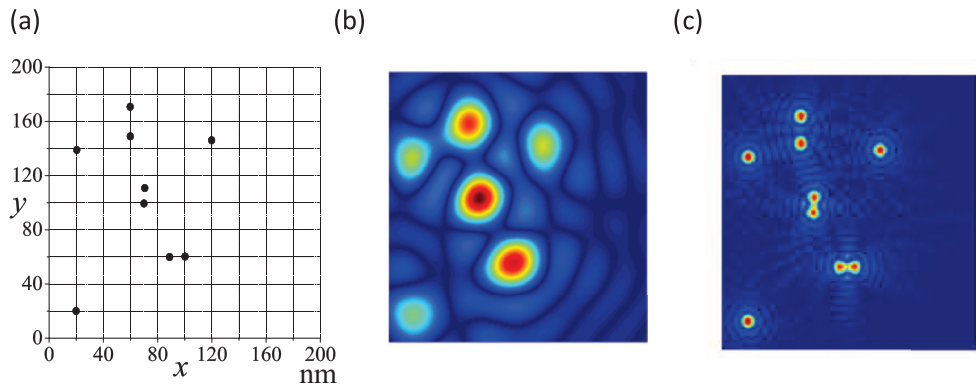


FIG. 3. (Color online) (a) The atom distribution. (b) The image simulation with $E_F = 0.4$, $\hbar\omega = 0.2 \text{ eV}$, $\varepsilon_1 = 2$, and $\varepsilon_2 = 2$. Here, $\text{Re}(k_{gp}) = 68.5k_0$. (c) The image simulation with $E_F = 0.6$, $\hbar\omega = 0.4 \text{ eV}$, $\varepsilon_1 = 3$, and $\varepsilon_2 = 3$. Here, $\text{Re}(k_{gp}) = 137k_0$.

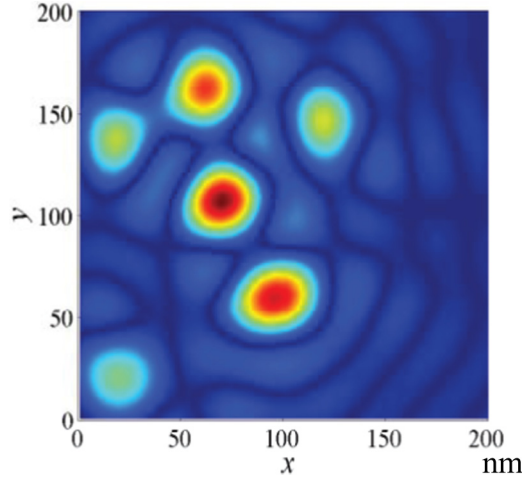


FIG. 4. (Color online) (a) The image simulation at the same conditions as in Fig. 3(b) but considering loss. At the origin point, the two GPs have the same intensity.

$e^{-ik_x x} e^{-ik_y y} dx dy$. Here, γ_x and γ_y are the imaginary parts of the plasmon wave vector along the x and y directions with $\sqrt{\gamma_x^2 + \gamma_y^2} = \text{Im}(k_{gp})$. We can obtain these components if $\gamma_x / \text{Re}(k_{gp}) \ll 1$. In our example, the Fourier transformation of the sample distribution is the coherent summation of the transformations of separated atoms' positions. The loss can affect the relative ratio between the Fourier components' amplitudes of a single atom, which induces the image of an atom not to be a circular spot. In experiment, the Fourier-transformation components in the circle located at the origin with radius κ can be obtained exactly by a conventional microscopy process. If we perform two observations with opposite y directions on the sample, the average Fourier components outside of the circle located at the origin with radius κ are $\iint F(x, y) (e^{-2\gamma_y y / 2} + e^{2\gamma_y y / 2}) e^{-i(k_x - k_1)x} e^{-ik_y y} dx dy$ and $\iint F(x, y) (e^{-2\gamma_y y / 2} + e^{2\gamma_y y / 2}) e^{-i(k_x + k_1)x} e^{-ik_y y} dx dy$. We assume that when the maximum loss enlarged Fourier-transformation amplitude is smaller than 1.2 times the original value, the effect of loss can be neglected. This means $e^{-2\gamma_y y / 2} + e^{2\gamma_y y / 2} < 1.2$. We can obtain that the sample size should be smaller than $2.5\alpha\mu E_F^2 / [\hbar(\epsilon_1 + \epsilon_2)k_0 e v_F^2]$. It follows, on comparing Fig. 4 with Fig. 3(b), that the influence of the loss is very small.

Of course, if the size of the sample is quite big compared to the GP wavelength, the dissipation effect discussed above cannot be neglected. To overcome this problem, we can utilize another energy level $|c\rangle$ of the sample atom, shown in Fig. 5(a). After the atom is excited to state $|e\rangle$, we use a pulse that is incident normal to the sample plane to drive the atom from $|e\rangle$ to $|c\rangle$. The GPs' pattern in the pulse domain can be considered to be sinusoidal. The field of the pulse section is Gaussian. As a result, after the pulse, the population of $|c\rangle$ in the pulse domain will present a shape with a maximum at the pulse center and will decrease away from the center. The distribution can be described as $G(x, y)$ depending on the field intensity and the decay rates of the atomic levels with a nonzero result only in the Gaussian pulse domain. The image result is equal to the case of replacing $F(x, y)$ in Eq. (2) with $F(x, y)G(x, y)$. We can

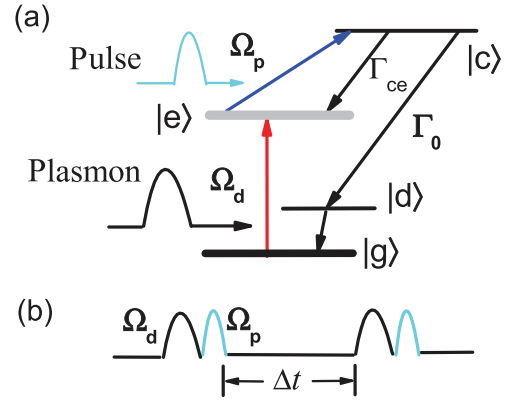


FIG. 5. (Color online) (a) The sample atom structure. The atom can decay from level $|c\rangle$ to $|e\rangle$ and $|d\rangle$ spontaneously with decay rates Γ_{ce} and Γ_0 , respectively. (b) Two pulses irradiate the sample periodically.

distinguish the atom at the position with $G(x, y)$ a little bigger than 0, which is in order to overcome the noise. In the imaging process, we use the photons emitted from $|c\rangle$ to $|d\rangle$ with frequency ω_{cd} for imaging. The probability to get a photon at frequency ω_{cd} is about $\Gamma_0 / (\Gamma_0 + \Gamma_{ce})$. Controlling the position of the Gaussian pulse, every time, we can reconstruct the image in the range of the pulse width. Changing the positions of the GPs and the Gaussian pulse, we can image all the sample. Additionally, $\omega_{cd} > \omega_{eg}$ means a larger κ and can lead to a faster imaging process.

With recent progress in the fabrication and manipulation of graphene, a mobility as large as $\mu = 10^{-5-6} \text{ cm}^2 \text{ V}^{-1} \text{ s}^{-1}$ can be achieved [23,24]. This results in a lower loss. In Fig. 1(c), we plot the field intensity with $\mu = 10^5 \text{ cm}^2 \text{ V}^{-1} \text{ s}^{-1}$. An almost perfect sinusoidal field pattern can be obtained, leading to higher precision.

Another problem is that the fluorescence photons may be absorbed by the graphene due to the strong coupling between the GPs and the emitters. To solve this problem, choosing the thickness h of the dielectric slab is important. We note that the coupling strength between the emitter and the plasmon decreases exponentially as the distance to the graphene plane increases [34]. We can therefore choose a relatively large h , and then most of the photons can be collected by the objective lens. Meanwhile, the illumination plasmons' intensity decreases rapidly as the slab thickness increases. We should therefore enlarge the illumination plasmons' intensity to make sure the field on the sample is strong enough to drive the atom.

In an experiment, the GPs pulse length can be chosen to be 1 ns and two pulses separation to be 30 ns, shown in Fig. 5(b), which is long enough to bring the atom back to the ground state. We assume a 0.1-photon collection efficiency. In 1 s, we can collect, on average, 3×10^6 photons from one atom. For the parameters in Fig. 3(c), we need about 10 000–15 000 images [15,16]. Adding the time for controlling the pulse phase and direction, our scheme also needs a relatively long time as in the conventional SIM, i.e., tens of seconds to minutes [16].

Comparing with the GPs, the surface plasmons based on a metal film have symmetry and antisymmetry eigenmodes. The symmetry mode has a small wave number associated with low-resolution ability. The antisymmetry mode has a

relatively large wave number. However, this mode also can be accompanied by large dissipation [36], which is harmful to be used in imaging. As a result, GPs have their evident advantages.

IV. CONCLUSION

In conclusion, we have proposed a linear scheme for subdiffraction microscopy by using the GPs due to their extremely small plasmon wavelength and low dissipation. An image with nanometer-scale resolution can be obtained under very weak light intensity, which is important in the imaging of the biological systems. The scheme is ultimately limited by the height of the sample [17,37,38] and is suitable for the

sample with nanometers or tens of nanometers height. Thus our system mainly shows its power in the interface system, such as analyzing biological molecular structures. Besides, SIM does not consider the dipole-dipole interaction. If the fluorescence atoms are too close, i.e., about 10 nm, the atoms can affect each other, so the maximum resolution capability of our scheme is about 10 nm.

ACKNOWLEDGMENTS

This research was supported by the National Priorities Research Program Grant No. 5-102-1-026 from the Qatar National Research Fund and a grant from King Abdulaziz City for Science and Technology.

-
- [1] E. Betzig, G. H. Patterson, R. Sougrat, O. W. Lindwasser, S. Olenych, J. S. Bonifacino, M. W. Davidson, J. L. Schwartz, and H. F. Hess, *Science* **313**, 1642 (2006).
 - [2] C. Hettich, C. Schmitt, J. Zitzmann, S. Kühn, I. Gerhardt, and V. Sandoghdar, *Science* **298**, 385 (2002).
 - [3] Z. Y. Liao, M. Al-Amri, and M. S. Zubairy, *Phys. Rev. A* **85**, 023810 (2012).
 - [4] J. T. Chang, J. Evers, M. O. Scully, and M. S. Zubairy, *Phys. Rev. A* **73**, 031803(R) (2006).
 - [5] J. T. Chang, J. Evers, and M. S. Zubairy, *Phys. Rev. A* **74**, 043820 (2006).
 - [6] S. Qamar, J. Evers, and M. S. Zubairy, *Phys. Rev. A* **79**, 043814 (2009).
 - [7] H. B. Li, V. A. Sautenkov, M. M. Kash, A. V. Sokolov, G. R. Welch, Y. V. Rostovtsev, M. S. Zubairy, and M. O. Scully, *Phys. Rev. A* **78**, 013803 (2008).
 - [8] M. J. Rust, M. Bates, and X. Zhuang, *Nat. Methods* **3**, 793 (2006).
 - [9] Z. Liu, H. Lee, Y. Xiong, C. Sun, and X. Zhang, *Science* **315**, 1686 (2007).
 - [10] V. Westphal and S. W. Hell, *Phys. Rev. Lett.* **94**, 143903 (2005).
 - [11] D. Wildanger, J. R. Maze, and S. W. Hell, *Phys. Rev. Lett.* **107**, 017601 (2011).
 - [12] T. A. Klar, S. Jakobs, N. Dyba, A. Egner, and S. W. Hell, *Proc. Natl. Acad. Sci. USA* **97**, 8206 (2000).
 - [13] M. G. L. Gustafsson, *J. Microsc.* **198**, 82 (2000).
 - [14] J. T. Frohn, H. F. Knapp, and A. Stemmer, *Proc. Natl. Acad. Sci. USA* **97**, 7232 (2000).
 - [15] R. Heintzmann, T. M. Jovin, and C. Cremer, *J. Opt. Soc. Am. A* **19**, 1599 (2002).
 - [16] M. G. L. Gustafsson, *Proc. Natl. Acad. Sci. USA* **102**, 13081 (2005).
 - [17] F. Wei and Z. Liu, *Nano Lett.* **10**, 2531 (2010).
 - [18] A. K. Geim and K. S. Novoselov, *Nature Mater.* **6**, 183 (2007).
 - [19] A. H. Castro Neto, F. Guinea, N. M. R. Peres, K. S. Novoselov, and A. K. Geim, *Rev. Mod. Phys.* **81**, 109 (2009).
 - [20] R. R. Nair, P. Blake, A. N. Grigorenko, K. S. Novoselov, T. J. Booth, T. Stauber, N. M. R. Peres, and A. K. Geim, *Science* **320**, 1308 (2008).
 - [21] J. Chen, M. Badioli, P. Alonso-González, S. Thongrattanasiri, F. Huth, J. Osmond, M. Spasenović, A. Centeno, A. Pesquera, P. Godignon, A. Z. Elorza, N. Camara, F. J. Garcia de Abajo, R. Hillenbrand, and F. H. L. Koppens, *Nature* **487**, 77 (2012).
 - [22] Z. Fei, A. S. Rodin, G. O. Andreev, W. Bao, A. S. McLeod, M. Wagner, L. M. Zhang, Z. Zhao, M. Thiemens, G. Dominguez, M. M. Fogler, A. H. Castro Neto, C. N. Lau, F. Keilmann, and D. N. Basov, *Nature* **487**, 82 (2012).
 - [23] Z. Fang, S. Thongrattanasiri, A. Schlather, Z. Liu, L. Ma, Y. Wang, P. M. Ajayan, P. Nordlander, N. J. Halas, and F. J. Garcia de Abajo, *ACS Nano* **7**, 2388 (2013).
 - [24] T. Low and P. Avouris, *ACS Nano* **8**, 1086 (2014).
 - [25] L. Ju, B. Geng, J. Horng, C. Girit, M. Martin, Z. Hao, H. A. Bechtel, X. Liang, A. Zettl, Y. R. Shen, and F. Wang, *Nat. Nanotechnol.* **6**, 630 (2011).
 - [26] M. Gullans, D. E. Chang, F. H. L. Koppens, F. J. Garcia de Abajo, and M. D. Lukin, *Phys. Rev. Lett.* **111**, 247401 (2013).
 - [27] A. N. Grigorenko, M. Polini, and K. S. Novoselov, *Nat. Photonics* **6**, 749 (2012).
 - [28] A. Vakil and N. Engheta, *Science* **332**, 1291 (2011).
 - [29] T. R. Zhan, F. Y. Zhao, X. H. Hu, X. H. Liu, and J. Zi, *Phys. Rev. B* **86**, 165416 (2012).
 - [30] B. Wunsch, T. Stauber, F. Sols, and F. Guinea, *New J. Phys.* **8**, 318 (2006).
 - [31] E. H. Hwang and S. Das Sarma, *Phys. Rev. B* **75**, 205418 (2007).
 - [32] S. A. Mikhailov and K. Ziegler, *Phys. Rev. Lett.* **99**, 016803 (2007).
 - [33] M. Jablan, H. Buljan, and M. Soljačić, *Phys. Rev. B* **80**, 245435 (2009).
 - [34] F. H. L. Koppens, D. E. Chang, and M. Soljačić, *Nano Lett.* **11**, 3370 (2011).
 - [35] X. H. Yao, M. Tokman, and A. Belyanin, *Phys. Rev. Lett.* **112**, 055501 (2014).
 - [36] B. Wang, X. Zhang, F. J. Garcia-Vidal, X. C. Yuan, and J. H. Teng, *Phys. Rev. Lett.* **109**, 073901 (2012).
 - [37] F. Balzarotti and F. D. Stefani, *ACS Nano* **6**, 4580 (2012).
 - [38] B. Gjonaj, J. Aulbach, P. M. Johnson, A. P. Mosk, L. Kuipers, and A. Lagendijk, *Phys. Rev. Lett.* **110**, 266804 (2013).